Arabian Journal of Chemistry (2021) **14**, 103359

King Saud University

Arabian Journal of Chemistry

www.ksu.edu.sa
www.sciencedirect.com

ORIGINAL ARTICLE

Facile synthesis of MIL-100 metal-organic framework via heatless technique for the adsorptive treatment of cationic and anionic pollutants

K.L. Tan, K.Y. Foo *

River Engineering and Urban Drainage Research Centre (REDAC), Engineering Campus, Universiti Sains Malaysia, Seri Ampangan, 14300 Nibong Tebal, Penang, Malaysia

Received 7 May 2021; accepted 26 July 2021
Available online 02 August 2021

KEYWORDS

Adsorption;
Dye;
Mechanism;
MIL-100;
MOF;
Pharmaceutical

Abstract The facile synthesis of an iron-based metal-organic framework, MIL-100(Fe) has been successfully conducted via a heatless water-based technique. The unique features have been evaluated with respect to the X-ray diffraction, field emission scanning electron microscopy, nitrogen adsorption-desorption analysis, Fourier transform infrared spectroscopy, and zero point of charge measurement. The adsorptive potential was examined using the cationic (methylene blue, MB) and anionic (naproxen, NPX) water pollutants. The synthesized MIL-100(Fe) sample, MIL-100 ($FeSO_4$), owned a crystalline microporous-mesoporous structure, with a large BET surface area of 1984 m^2/g and total pore volume of 1.096 cm^3/g. The equilibrium data best conformed to the Langmuir-Freundlich isotherm and pseudo-second order kinetic model, with the maximum adsorption capacity for MB and NPX of 568.1 mg/g and 148.8 mg/g, respectively. Thermodynamic analysis revealed the favorable energetics ($\Delta G < 0$ and $\Delta S > 0$), endothermic ($\Delta H > 0$ for MB) and exothermic nature ($\Delta H < 0$ for NPX) of the adsorption process. Negligible degradation of the adsorptive performance was recorded under high ionic strength solutions and simulated wastewaters. MIL-100($FeSO_4$) demonstrated great regenerative potential by ethanol stripping for at least 5 regeneration cycles. The present findings provide an invaluable insight into the green synthesis technique of MIL-100(Fe), with high upscaling prospects. Imparted with different surface anionicity and electrically neutral functional sites, MIL-100($FeSO_4$) has emerged to be a potent adsorbent for the successful treatment of both cationic and anionic water pollutants, even under high-strength water samples with complex water matrices.

* Corresponding author.
E-mail addresses: tankeeliew@gmail.com (K.L. Tan), k.y.foo@usm.my (K.Y. Foo).

Peer review under responsibility of King Saud University.

Production and hosting by Elsevier

1. Introduction

Today, the excessive applications of synthetic chemicals from the rising industrial, agricultural and household demands, and the ubiquitous presence of these hazardous contaminants in the natural water body, remain the most critical global agenda. Among all, dyes constitute the major class of water

https://doi.org/10.1016/j.arabjc.2021.103359
1878-5352

pollutants, with an annual production rate exceeding 7×10^5 tons (Pathania et al., 2017). Contrasting the traditional priority pollutants, pharmaceuticals and personal care products are renowned as the "emerging pollutants", due to their short history of detections in the natural environment. Non-steroidal anti-inflammatory drugs (NSAIDs), a major class of pharmaceuticals, could be endocrine disrupting compounds (He et al., 2017). Within this context, the establishment of an affordable and green treatment technique is urgently required.

Experiencing a rapid revolution for the past twenty years, metal-organic frameworks (MOFs) have evolved to be one of the most promising class of materials, serving an ever-broadening spectrum of applications (Ryu et al., 2021). MOFs or porous coordination polymers, are 3-D network-like crystalline constructs that consist of metal ions or metal ions clusters, bridged by multitopic organic ligands in space. Their unparalleled popularity stems from their well designability, large specific surface area, regular guest-accessible pore space, ease of functionalization, and high thermal stability (Seetharaj et al., 2019). Specifically, MOF materials have been craftily engineered for the remediation of various kinds of water pollutants (Peng et al., 2018; Tang et al., 2020). On the same note, the designed fabrication of zeolike-like metal-organic frameworks (ZMOFs), a subclass of MOFs, has become a new avenue to the zeolitic architectures of MOF materials, integrating both the advantages of conventional zeolites and MOFs. A unique ZMOF is MIL-100(Fe), with a zeolitic MTN rigid crystal structure of $[Fe_3^{III}O(H_2O)_2(F/OH)\cdot\{C_6H_3(CO_2)_3\}_2]$ (Scheme 1). MIL-100(Fe) can be conceptually simplified to the zeotypic MTN architecture derived from the high-silica zeolite ZSM-39. Specifically, MIL-100(Fe) consists of a hierarchy of accessible cage-type pores: the micro-pocket (the ST, Ø ≈7 Å), the small *meso*-cage (Ø ≈25 Å) and the big *meso*-cage (Ø ≈29 Å). MIL-100(Fe) is highly appreciated for its structural stability and non-toxicity, which further enhances the additional value of MOF, and drives its advances into the aqueous phase and bio-related applications.

Since the first report on the HF- and HNO_3-assisted synthesis of MIL-100(Fe) at 150 °C for 6 days in 2007 (Horcajada et al., 2007), research efforts to steer the preparation of MIL-100(Fe) towards greener conditions have been growing rapidly, leading to microwave-assisted synthesis (Aguiar et al., 2020), reflux synthesis (Ozer et al., 2020), mechanochemical synthesis (Han et al., 2017), dry gel conversion (Luo et al., 2019), and lately, water-based synthesis (So et al., 2020), using nitrate or chloride salts as the iron source. This detracts from the up-scalability because nitrates make oxidative hazards, while chlorides pose corrosive risks to the metal-based reactors during the industry-scale manufacturing processes (Julien et al., 2017).

In this work, MIL-100(Fe) has been synthesized via a water-based heatless approach by adopting $FeSO_4{\cdot}7H_2O$ as the iron (III) precursor, a safer choice for the upscaling requirement. The morphological, structural, textural, functional and surface chemical properties of MIL-100($FeSO_4$) were evaluated. The adsorptive potential was examined with respect to a cationic dye (methylene blue, MB) and an anionic NSAID (naproxen, NPX) pollutants. This sustainably synthesized MIL-100($FeSO_4$) preserved the highly desirable traits against the conventional MIL-100, and recorded a remarkable adsorptive performance for cationic MB and anionic NPX. The present study showcases the simplistic engineering of a MOF-derived adsorbent, which is versatile for the effective sequestration of both cationic and anionic adsorbates under

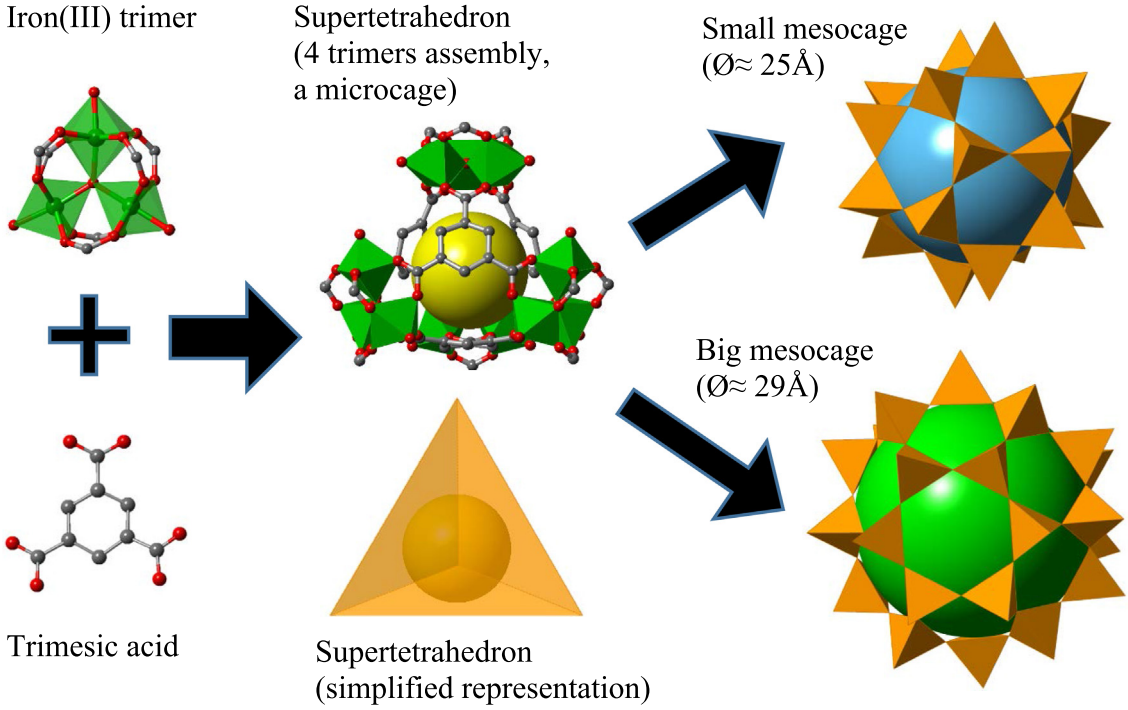

Scheme 1 The zeolite-like MTN hierarchical pore structure of MIL-100(Fe). Four trimers and four linkers form a supertetrahedron (ST), which is a micro-cage. 20 ST units are joined together by sharing vertices to form the small meso-cage, and 28 ST units form the big meso-cage. The colored spheres inside the cages are the imaginary objects drawn to mark the internal free volume.

different settings. The sustainable water-based heatless synthesis technique and high reusability ascertained the real practicability of MIL-100($FeSO_4$) as a prevailing alternative to the available functionalized adsorbents.

2. Materials and methods

2.1. Chemicals and solvents

All reagents applied in this work were of analytical reagent grade or higher purity. Iron(II) sulfate heptahydrate ($FeSO_4{\cdot}7H_2O$, ≥99%), trimesic acid (TMA, ≥95%), sodium hydroxide pellets (NaOH, ≥98.4%), absolute ethanol (≥99.9%), acetone (≥99.5%), methylene blue (MB), naproxen (NPX) were used as purchased. Double distilled water was used in each individual experiment, and the molecular structures and dimensions of MB and NPX are provided in Table S1. MB and NPX were adopted as the representative model cationic and anionic water pollutants, due to their high environmental relevance, with extremely high persistency and recalcitrance towards biodegradation in nature. The different characteristics of these model adsorbates make them the ideal inputs for the effective verification of the functional versatility.

2.2. Preparation of MIL-100($FeSO_4$)

The preparation procedure was adopted from Guesh et al. (2017) with slight modifications, whereby the TMA (1.9 g, 9.1 mmol) was stirred vigorously to be dissolved in 30 cm^3 of aqueous NaOH (1.0 M). This TMA solution was added dropwise to an iron(II) salt solution, which has been prepared beforehand by dissolving $FeSO_4{\cdot}7H_2O$ (3.8 g, 13.7 mmol) in 120 cm^3 water. The solution mixture was stirred for 24 h to allow for crystallization under ambient temperature. The gradual change of solution color from yellowish-green to orange and dark brown signified the formation of MIL-100(Fe) crystals. The orangish-brown powder was collected via centrifugation and washed sequentially with water and ethanol for the neutralization of solution pH and removal of unreacted ingredients. The purified MIL-100(Fe) sample, denoted as MIL-100($FeSO_4$), was dried in an oven at 60 °C.

2.3. Physical and chemical characterizations

The crystalline identity of MIL-100($FeSO_4$) was investigated by X-ray diffraction (XRD) using a Bruker D8 Advance diffractometer, with monochromatic Cu Kα radiation (λ = 1.5406 Å) at 40 kV and 40 mA. The morphology of the crystalline MOF sample was visualized by using the field emission scanning electron microscopy (FESEM) instrument (ZEISS Supra 35VP, Germany) at an accelerating voltage of 5.0 kV. The Fourier transform infrared (FTIR) spectra were recorded with an IR spectrophotometer (Perkin Elmer Spectrum One, USA) at a resolution of 4 cm^{-1}, by adopting the standard KBr disk method. Elemental analysis was conducted by CHNS/O elemental analyzer (Perkin Elmer 2400 series II, USA). The textural properties of the solid sample were ascertained by the nitrogen adsorption–desorption technique at −196 °C by using the Micromeritics ASAP 2020 (USA) analyzer. Prior to the analysis, the sample was degassed at 120 °C for 5 h. From the N_2 adsorption isotherm, the specific surface area was deduced by the Brunauer-Emmett-Teller (BET) method, while the pore size distribution was predicted by the Barrett-Joyner-Halenda (BJH) method.

Point of zero charge (pH_{pzc}) was determined by the solid addition method. To each Erlenmeyer flask, 50 mL of 0.1 M NaCl aqueous solution was added. The initial pH values (pH_i) of the salt solutions were adjusted to the pH 2–12 by adding drops of 0.1 M HCl or NaOH. 0.05 g solid adsorbent was added to each flask, and the solid–liquid mixtures were agitated at 30 °C for 48 h. The final equilibrium pH values (pH_f) were measured, and plotted against the pH_i values, and its intersection with the y = x line was taken as the pH_{pzc}.

2.4. Batch adsorption experiments

The batch adsorption experiments were carried out by agitating 0.1 g of MIL-100($FeSO_4$) in 200 mL of MB solutions within the concentration range from 50 to 500 mg/L, and NPX solutions within the concentration range of 10–100 mg/L. The smaller range of study for NPX concentrations was due to its limited solubility in aqueous solution. Working solutions were prepared by diluting the standard stock solutions at the initial concentration of 1000 mg/L for MB and 100 mg/L for NPX. The adsorption kinetic study was conducted by withdrawing the aliquot samples at different time intervals, and the residual concentration was examined using a UV–visible spectrophotometer (Shimadzu UV-1800, Japan). The pollutant uptake at time t (min), q_t (mg/g) and at equilibrium, q_e (mg/g) were defined as:

$$q_t = \frac{(C_o - C_t)V}{m} \tag{1}$$

$$q_e = \frac{(C_e - C_t)V}{m} \tag{2}$$

where C_o, C_t and C_e are the pollutant concentration (mg/L) at initial, time t, and at equilibrium, respectively; V is the solution volume (mL), and m is the mass of adsorbent (mg). To evaluate the effect of adsorbent dosage, the adsorbent dosage was varied from 0.05 g/L to 1.2 g/L. For the assessment of changing solution pH, the initial pH was adjusted to pH 2 − pH 11 by adding drops of $NaOH_{(aq)}$ or $HCl_{(aq)}$. The removal efficiency is given as:

$$\textit{Removal efficiency}\ (\%) = \frac{(C_o - C_e)}{C_o} \times 100\% \tag{3}$$

The spent MIL-100($FeSO_4$) sample was regenerated by solvent washing under ultrasound for 30 min, by adopting ethanol and acetone as the regenerating solvents. The adopted mass-to-volume ratio during the regeneration stage is 0.6 g MOF per 100 mL of regenerant. The regenerated MIL-100($FeSO_4$) was dried at 60 °C in an oven.

3. Results and discussion

3.1. Characterization

Scanning electron microscopy (SEM) provides a real-time visualization of the sample down to the sub-micron scale to enable a detailed observation of the surface morphology and particle size of the functionalized adsorbent. The morphology of MIL-100($FeSO_4$), as observed in Fig. 1(a), demonstrates a

polycrystalline structure, containing intergrown octahedral crystallites with different sizes between 0.5 and 1.0 μm. Featured by well-defined facets and edges with an octahedral exterior, the MIL-100($FeSO_4$) particles clearly manifested the surface morphological character of a crystalline entity. The crystallite size distribution fell into such a narrow domain, due to the regulated crystal nucleation that was restricted to a short time frame by the NaOH additive during the water-mediated crystallization process. The crystal structure of the product adsorbent was analyzed by XRD, and compared to the simulated X-ray diffraction pattern of a standard MIL-100 structure, which was generated by the program MERCURY using the crystallographic data file retrieved from the Cambridge Structural Database via CSD-Refcode CIGXIA. As depicted in Fig. 1(b), the diffraction peaks of the product MOF matched well with those expected of a MIL-100 crystal. The product adsorbent could be ascertained to be a crystalline material of MIL-100-type structure. The three most prominent Bragg peaks were well-observed at 2θ≈6.26°,10.20°, and 10.98°, corresponding to the lattice planes of (5 1 1), (8 2 2) and (7 5 3), respectively, while other peaks detected at 2θ≈5.24, 5.90, 6.80,7.11,12.55, and 20.06° were produced by the (3 3 1),

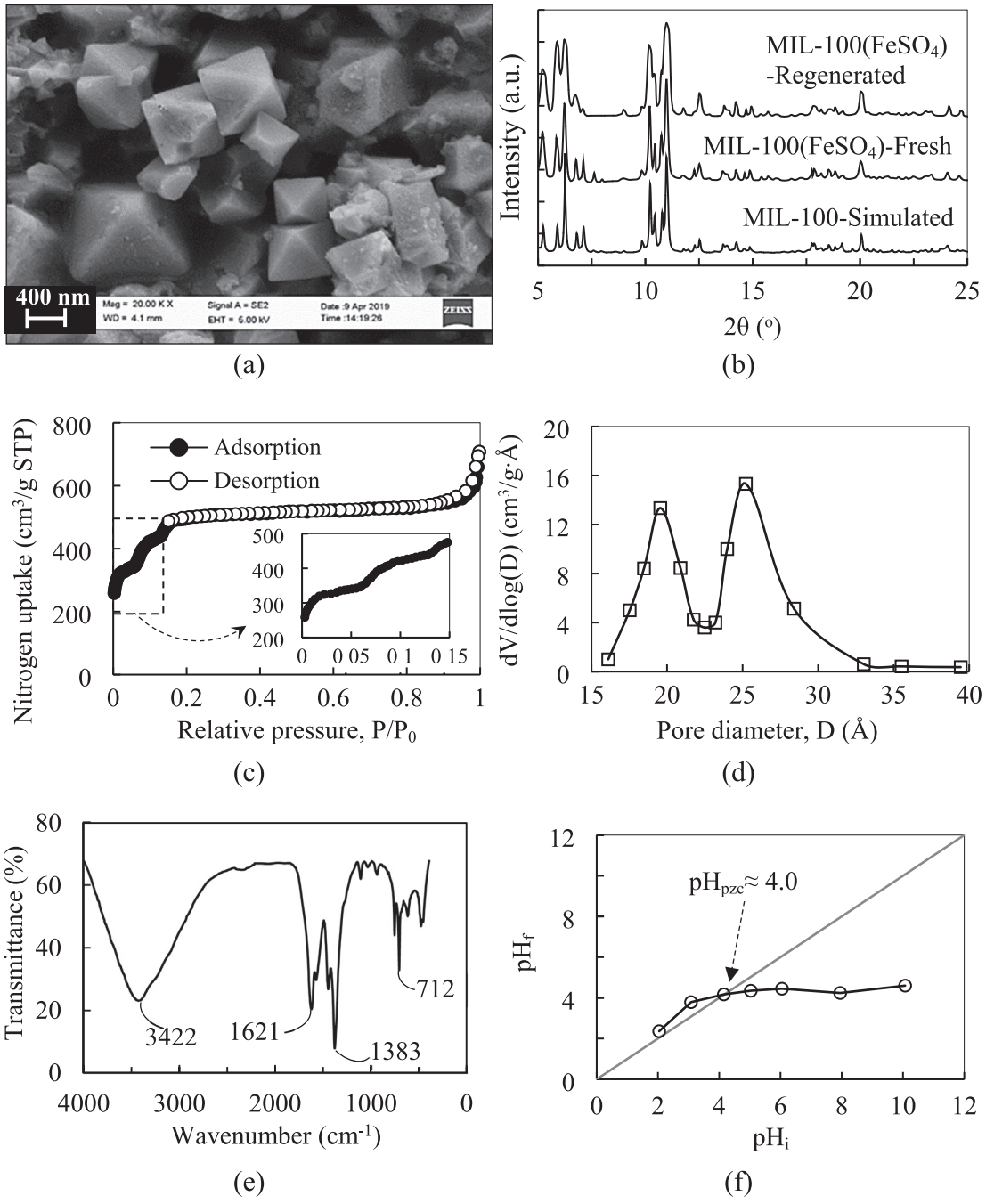

Fig. 1 Physical and chemical characterizations of MIL-100($FeSO_4$): (a) SEM, (b) XRD, (c) N_2 adsorption–desorption at −196 °C, (d) pore size distribution, (e) FTIR, and (f) point of zero charge.

(422), (440), (531), (862), and (1395) planes, respectively, within the crystal structure of MIL-100($FeSO_4$). The absence of spurious peaks points to the phase purity of the synthesized sample.

The nitrogen adsorption–desorption isotherms were a composite of Type-I and Type-IV isotherms, as given in Fig. 1 (c). According to the International Union of Pure and Applied Chemistry (IUPAC) classification, Type-I isotherm indicates a microporous system (Pore size < 2 nm), while Type-IV which bears a hysteresis loop, signifies a mesoporous system (2 nm < Pore size < 50 nm) (Thommes et al., 2015). The secondary uptakes of nitrogen at $P/P_0 \approx 0.06$ and 0.14 further evidenced the presence of both microporous and mesoporous structure of the MOF. Below $P/P_0 \approx 0.06$, the microcavities filling (0.7 nm) was mainly responsible for the nitrogen uptake. The onset of the first secondary uptake marked the beginning of the filling of the small mesocavities (2.5 nm), while the next secondary uptake indicated the occupation of the big mesocavities (2.9 nm). The Brunauer Emmet Teller (BET) surface area, total pore volume, and average pore width of MIL-100($FeSO_4$) were identified to be 1984 m^2/g, 1.096 cm^3/g, and 2.29 nm, respectively (Table 1). MIL-100($FeSO_4$) contains a balanced mix of hierarchically organized micropores and mesopores, with a mesopore volume to micropore volume ratio of approximately 55:45, and a mesopore surface area to micropore surface area of ca. 45:55. The Barrett-Joyner-Halenda (BJH) pore size distribution (Fig. 1(d)) of MIL-100($FeSO_4$) exhibited two peaks at ~ 2.0 nm and ~ 2.5 nm. These values were ~ 0.4 nm smaller than the corresponding crystallographic values, probably due to the BJH methodology that tends to underestimate the mesopore sizes. In a nutshell, the high surface area and the large pore volume centered around the lower mesoporous regime with significant microporosity for closer guest confinement are particularly desirable for the pore transport and adsorption of bulky substrates, including dye molecules.

FTIR spectroscopy is an instrumental analysis technique for the detection of organic functionalities and the chemical bonding within the solid adsorbent. This information is important for the full description of the molecular compositions and structural features of the functionalized material. The FTIR spectrum of MIL-100($FeSO_4$) is recorded in Fig. 1(e). The intense peaks at 1621 cm^{-1} and 1383 cm^{-1} could have been produced by the asymmetric stretching of the carboxylate (ν_{as}(O═C─O$^-$)) and symmetric stretching (ν_s(O═C─O$^-$)) of the carboxylate moiety of TMA. Meanwhile, the intensity at 1710–1720 cm^{-1} assigned to the C═O stretching of free TMA was not detected (Han et al., 2017), while the ν(Fe─O) peak was found at 712 cm^{-1} (Cai et al., 2016), to ascertain that the unreacted TMA species has been removed effectively in the purification step, and the TMA molecules were coordinated to the iron atoms of the MOF framework. Similarly, the undetectable O═S═O bonds between 1170 and 1260 cm^{-1} from the FTIR spectrum further verified that SO_4^{2-}, the counteranion of the iron source, has been removed completely from the MOF surface (Juan-Alcañiz et al., 2013). The finding was well corroborated with the elemental analysis, as depicted in Table S2. The signal at 3422 cm^{-1} is related to the O─H stretching, which could be the O─H groups of the aqua ligands coordinated to the Fe^{III} atoms. From Fig. 1(f), the pH point of zero charge for the surface charge neutrality is pH ~ 4.0, above which the MIL-100($FeSO_4$) surface was negative charged. The wide pH domain above pH 4.0 for which the adsorbent surface bears a net negative charge lays an electrical advantage for MIL-100($FeSO_4$) to interact electrostatically with the opposite-charged adsorbates.

Table 1 Textural parameters of MIL-100($FeSO_4$).

Textural property	Description
BET surface area[a] (m^2/g)	1984
Langmuir surface area (m^2/g)	2437
External surface area[b] (m^2/g)	92
Micropore surface area[c] (m^2/g)	1003
Mesopore surface area (m^2/g)	889
Total pore volume[d] (cm^3/g)	1.096
Micropore volume[b] (cm^3/g)	0.481
Mesopore volume (cm^3/g)	0.615
Average pore width[e] (nm)	2.29

[a] Evaluated at the range $0.05 < P/P_0 < 0.20$.
[b] t-plot method.
[c] Estimated from the crystallographic MIL-100 model after deducting S_{ext}.
[d] Evaluated at point $P/P_0 = 0.99$.
[e] BJH method applied to the desorption branch.

3.2. Effect of initial concentration and contact time

The adsorptive uptakes of MB and NPX have been examined at the initial concentration range of 50–500 mg/L and 10–100 mg/L, respectively, as illustrated in Fig. 2 (a, b). Generally, increasing the initial concentrations resulted in not only a greater initial uptake rate, but also a higher equilibrium uptake. Across the concentration range of 50–500 mg/L for MB and 10–100 mg/L for NPX, the experimental equilibrium uptake for MB and NPX increased 4.5 times and 6.8 times, respectively. Initial concentration represents a stronger driving force to overcome the mass transfer resistance, firstly across the external film of the MIL-100($FeSO_4$) particle to diffuse into the internal pore channels of MIL-100($FeSO_4$). The adsorptive uptake was rapid at the initial stage, due to the binding of the dye and drug adsorbates at the external surface, and with the lapse of time, the external surface turned saturated, and adsorbates diffusion into the pore channels commenced. Macroscopically, at this point, the adsorptive uptake profiles witnessed a slowdown, which eventually approached to a plateau, known as equilibrium. During this stage, the adsorption process is dynamic, whereby the rate of adsorptive uptake to the binding surface is equal to the rate of the adsorbate desorption. From Fig. 2, the equilibrium time for the adsorptive uptake of MB and NPX ranged within 120–160 min, and 50–140 min, respectively. Despite the requirement of a comparably longer equilibrium time, the adsorptive uptake of MB was kinetically favorable against NPX. At the initial concentration of 100 mg/L, the kinetic rate constant k_2 of MB was 2.6 times higher than NPX, indicating a kinetic advantage for MB over NPX as a guest over the MIL-100 ($FeSO_4$) binding sites. Similarly, the 50% of saturation degree was achieved within 3 min for the adsorptive uptake of MB, while the same loading for NPX took approximately 15 min. Accordingly, the smaller molecular size, higher symmetry

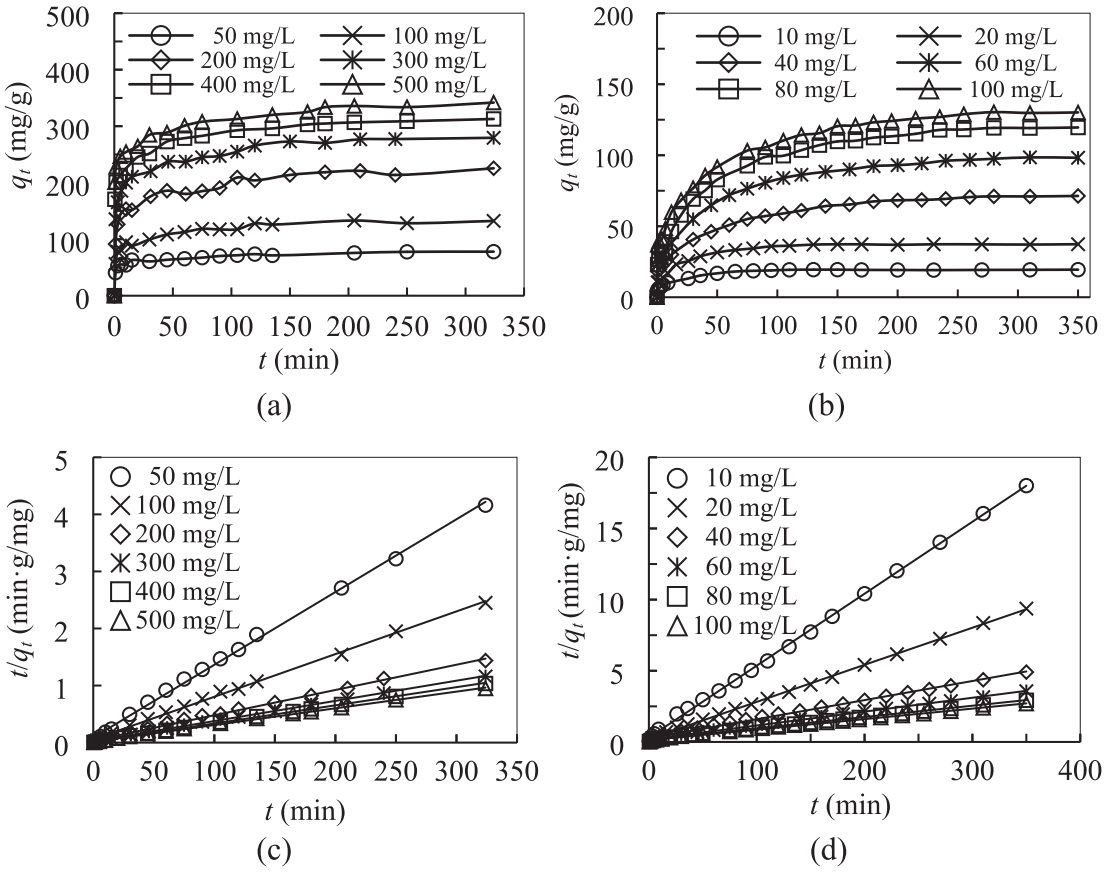

Fig. 2 Effect of initial concentration and contact time for the adsorptive uptake of (a) MB and (b) NPX onto MIL-100($FeSO_4$), and the corresponding plots of pseudo-second order kinetic model for (c) MB and (d) NPX at 30 °C.

and linear shape of MB molecules could be a governing factor of the kinetic behavior difference of the adsorption process.

3.3. Effect of adsorbent dosage and solution pH

Adsorbents which can accomplish an excellent cleaning performance at the minimum dosage is very much desirable in the real practical applications, with respect to the cost of adsorbents and regenerative potential. The adsorptive uptakes of MB and NPX onto MIL-100($FeSO_4$) as a function of adsorbent dosage are given in Fig. 3. Generally, increasing the adsorbent dosage showed a rising uptake rate, and recorded the optimum uptake rate at 0.2 g/L. Further increase in the adsorbent dosage beyond the optimum dosage resulted in a slight increase in the removal efficiency, while the adsorptive uptake took an opposite trend, and sustained an exponential reduction. The higher removal rate at a higher adsorbent dosage could be mainly attributed to the greater abundance of available active adsorption sites. The degree of removal increased gradually with the rising adsorbent dosage, and while the solid dosage turned extremely high, the available vacant surface active sites may not be accessible by the adsorbate molecules, due to the particles aggregation and solids dispersion effects. This undesirable aggregation of adsorbent particles sets a practical limit to the maximum removal rate, and represents the adsorbent utilization efficiency, witnessed by the plunge in the gravimetric uptakes.

The solution pH is a critical parameter, which exerts profound influence on the adsorptive uptake of charged adsorptive molecules onto the adsorbent surface due to the charge ionization state of the adsorbent surface and adsorbate molecules. It was clearly revealed from Fig. 3(c) and (d) that the aqueous pH showed an entirely opposite effect for the adsorptive uptakes of MB and NPX. The strong pH dependence of the adsorption process indicates electrostatic interaction as one of the major governing mechanisms. The adsorptive uptake of MB increased with the rising pH from the acidic (pH = 2) into the alkaline region (pH = 11). Generally, MB is a cationic dye, and it could be readily dissolved in water to produce a positive-charged species. At the solution pH < 4.0, which is the isoelectric point of the solid MIL-100 ($FeSO_4$) (Fig. 1(f)), the positive-charged solid surface would repel the like-charged dye species, resulting in a lower adsorptive uptake of MB. Progressing into the higher pH above 4.0, the adsorbent surface turned negatively charged, and hence afforded a greater electrostatic attractive force. Within the pH range from 4 to 12, the NPX-MIL-100($FeSO_4$) interaction was electrostatically disfavored, considering the pKa of NPX (4.2) and the pH_{pzc} of MIL-100($FeSO_4$) (4.0). At the solution pH < 4.0, the protonated carboxylate of NPX could form the H-bonding with MIL-100($FeSO_4$) as both H-donor and

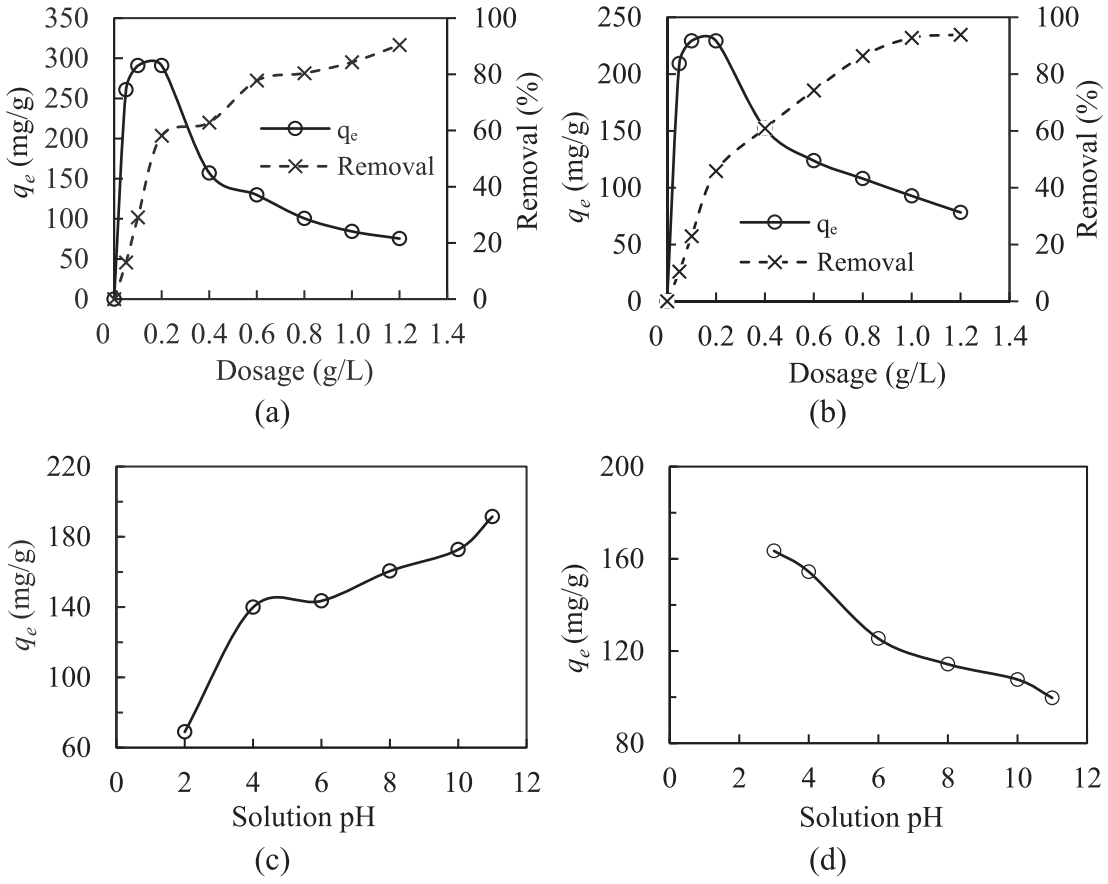

Fig. 3 Effect of adsorbent dosage and solution pH for the adsorptive uptake of MB (a, c) and NPX (b, d) onto MIL-100($FeSO_4$) (T = 30 °C, m/V = 0.5 g/L, C_o = 100 mg/L).

H-acceptor, thereby accounting for the elevated uptake under high-acidity conditions.

3.4. Batch adsorption equilibrium

At the equilibrium stage of the adsorption process, the distribution of the adsorbate molecules between the solid adsorbent and the bulk liquid phase could be correlated by the isotherm models. The establishment of adsorption equilibrium model represents both theoretical and practical significance, in a sense that it not only lends mechanistic insight into the adsorption system behavior, but also constitutes a crucial mathematical element in the process optimization and plant design. In this work, the equilibrium data were fitted to three isotherm models: Langmuir (Langmuir, 1916), Freundlich (Freundlich, 1906) and Langmuir-Freundlich (Sips, 1948) isotherms (Fig. 4). The fitted isotherm parameters are summarized in Table 2. The Langmuir isotherm is the most extensively employed isotherm, whereby the equilibrium uptake, q_e (mg/g) is related to the equilibrium concentration in the bulk liquid phase, C_e (mg/L), given by:

$$q_e = \frac{Q_o K_L C_e}{1 + K_L C_e} \tag{4}$$

where Q_o and K_L are denoted to the monolayer saturation adsorption capacity (mg/g) and the Langmuir isotherm constant (L/mg), respectively. Langmuir isotherm is an ideal localized monolayer model, and according to this model, the solid adsorbent contains only a finite number of well-defined active sites with uniform distribution of energy, with no transmigration or lateral interaction between the adsorbed molecules.

Conversely, Freundlich isotherm is the best-known isotherm for multilayer adsorption. It considers a non-ideal interaction, with the multiple active sites of the adsorbent surface, and successive binding to the bound layer, with the formation of multilayer adsorption. The equilibrium uptake is theoretically infinite according to the unlimited multilayer interaction, formulated as:

$$q_e = K_F C_e^{1/n_F} \tag{5}$$

where K_F is the Freundlich isotherm constant $\left[\left(\frac{\text{mg}}{\text{g}}\right)\cdot\left(\frac{\text{L}}{\text{mg}}\right)^{1/n_F}\right]$ and n_F is the heterogeneity factor related to the adsorption intensity.

The Langmuir-Freundlich (L-F) or Sips isotherm is a hybrid of the Langmuir and Freundlich isotherm models:

$$q_e = \frac{Q_S K_S C_e^{1/n_S}}{1 + K_S C_e^{1/n_S}} \tag{6}$$

where Q_S is the maximum adsorption capacity (mg/g); K_S is the L-F isotherm constant $\left[\left(\frac{L}{mg}\right)^{1/n_S}\right]$, and n_S is the heterogeneity factor. If n_S is approaching unity, the adsorptive

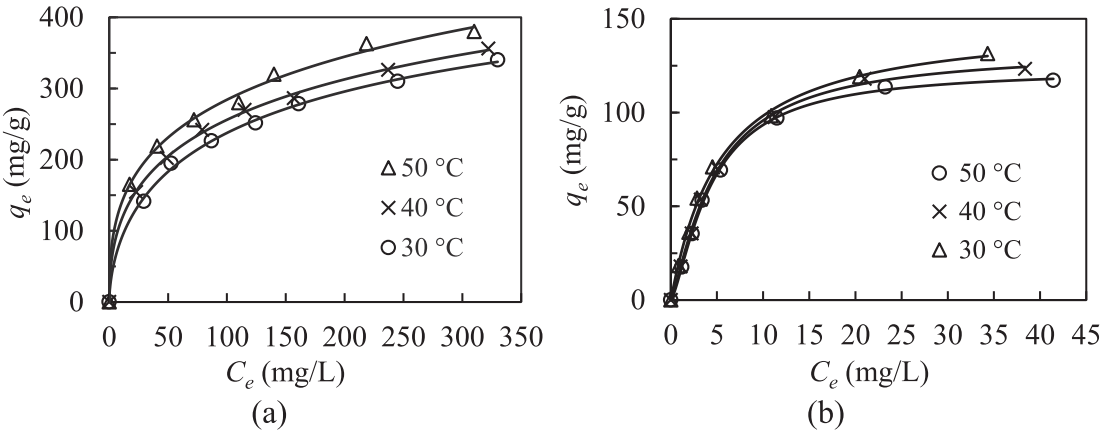

Fig. 4 Equilibrium isotherms for the adsorptive uptake of (a) MB and (b) NPX onto MIL-100($FeSO_4$).

Table 2 Isotherm parameters for the adsorptive uptakes of MB and NPX onto MIL-100($FeSO_4$).

Adsorbate	T (°C)	Langmuir			Freundlich			Langmuir-Freundlich			
		Q_o (mg/g)	K_L (L/mg)	R^2	$K_F\left[\left(\frac{mg}{g}\right)\cdot\left(\frac{L}{mg}\right)^{1/n_F}\right]$	n_F (L/mg)	R^2	Q_S (mg/g)	$K_S\left[\left(\frac{L}{mg}\right)^{1/n_S}\right]$	n_S	R^2
MB	30	380.94	0.018	0.993	47.604	2.900	0.995	568.06	0.046	1.680	0.999
	40	381.67	0.024	0.988	61.770	3.290	0.998	765.62	0.061	2.177	0.999
	50	403.10	0.029	0.977	70.821	3.363	0.996	1099.44	0.058	2.568	0.997
NPX	30	151.59	0.181	0.998	34.176	2.502	0.967	148.82	0.180	0.967	0.998
	40	147.27	0.166	0.995	32.951	2.568	0.943	133.42	0.142	0.799	0.999
	50	138.91	0.173	0.991	32.748	2.696	0.929	123.27	0.131	0.725	0.999

characteristics could be approximated to the Langmuir isotherm model. The L-F maximum capacity Q_S could be deduced at infinitely high concentration of adsorbates, when multilayer formation reaches its maximum limit.

From Table 2, despite the satisfactory fitting ($R^2 > 0.90$) to both Langmuir and Freundlich isotherm models, the hybrid L-F hybrid isotherm provided the best fitting for the adsorptive uptakes of MB and NPX, indicating the heterogeneous adsorption energies that arise from different active sites of both adsorbent and adsorbate interaction. This heterogeneity findings implied that multiple functional groups were involved in the pollutants binding, via multiple adsorptive mechanisms. The larger n_S values for MB reflected the higher heterogeneity of its chemical composition (C, H, N, S) and functionality over NPX (C, H, O).

Although both of these adsorption systems could be best described by the Langmuir-Freundlich hybrid behavior, the MIL-100($FeSO_4$)/MB adsorption was more of a Freundlich system, while MIL-100($FeSO_4$)/NPX adsorption tended to be Langmuirian, judging from their comparative R^2 values. The aforementioned result indicates: (i) multilayer adsorption is more feasible in the MIL-100($FeSO_4$)/MB system, (ii) the MIL-100($FeSO_4$)/MB system is more heterogeneous than the MIL-100($FeSO_4$)/NPX system. The first implication could be attributed to the molecular shape of MB, which is symmetrically flat plate-like for better multilayer stacking within the pore channels of MIL-100($FeSO_4$). The second implication arises from the higher structural and compositional heterogeneity of the MB molecule. Aromatic rings aside, the organic functionalities are heterocyclic N, heterocyclic S, and tertiary amine, which are more diverse than the ether and carboxylate moieties in NPX. This inherent heterogeneity of the MB structure allows heterogeneous adsorption, with different adsorption energy. The detailed pollutant-to-MOF binding mechanisms have been further explained in Section 3.9.

The rising temperature demonstrated a strong positive effect for the adsorption of MB, but showed a minor negative impact to the adsorptive uptake of NPX. Increasing the solution temperature from 30 °C to 50 °C has significantly boosted the monolayer capacity of MB from 568.06 mg/g to 1099.44 mg/g, but slightly reduced the monolayer capacity of NPX from 148.82 mg/g to 123.27 mg/g. Thermal energy is believed to have imparted extra kinetic mobility for the adsorbates to overcome the mass transfer resistance, and access the deepest micropores, resulting in a capacity enhancement. The linear-shaped and smaller molecular configuration of MB promised a less-obstructed pore transport and deeper pore access. Conversely, the boosting effect of thermal energy on NPX could have been slightly outweighed by its weakening effect on physical hydrogen bonding, which has been identified as the predominant adsorbent-binding mechanism of NPX (Section 3.9).

A comparison between the monolayer adsorption capacity of state-of-the-art adsorbents, specifically carbon nanotube, graphene oxide, graphene, clay, zeolite, metal oxide, organic polymer, biomass and their composites materials, is listed in Table 3. The synthesized MIL-100($FeSO_4$) compared favorably against other functionalized adsorbents as reported by

Table 3 Comparison of monolayer adsorption capacity for MB and NPX with different state-of-the-art adsorbents.

Adsorbate	Adsorbent	Best-fit isotherm model	T (°C)	Monolayer capacity (mg/g)	Reference
MB	**MIL-100($FeSO_4$)**	**Langmuir-Freundlich**	**30**	**568**	**This work**
			50	**1099**	
	Nucleotide@ZIF-8	Langmuir	25	10	Wu et al. (2021)
	Polyurethane-derived activated carbon foam	Langmuir	25	592	Udayakumar et al. (2021)
	Carboxymethyl-cyclodextrin-modified graphene oxide	Langmuir	25	246	Zhao et al. (2020)
	β-cyclodextrin-graphene oxide aerogel microspheres	Langmuir	25	438	Nie et al. (2021)
	Tannic acid functionalized graphene hydrogel	Langmuir	25	1000	Yao et al. (2021)
	Asparagine-multiwalled carbon nanotube	Langmuir	25	500	Saxena et al. (2021)
	ZnO-g-C_3N_4@PAA(HEC/PVA)-Fe^{3+}	Langmuir	25	325	Sultan et al. (2021)
	$SrFe_{12}O_{19}$@NaP1 zeolite	Freundlich	25	72	Cheng et al. (2021)
	Chitosan-montmorillonite/polyaniline	Temkin	25	111	Minisy et al. (2021)
	Bi_2O_3-SrO-FeO@SiO_2	Langmuir	25	244	Alomar et al. (2021)
	Sponge-gourd fibers/hydroxyapatite composite	Langmuir	25	25	Oun et al. (2021)
	EDTAD-modified magnetic baker's yeast	Langmuir	25	216	Xia et al. (2019)
NPX	**MIL-100($FeSO_4$)**	**Langmuir-Freundlich**	**30**	**149**	**This work**
			50	**123**	
	UiO-66	Langmuir	25	44	Bayazit and Şahin (2020)
	MIL-100(Fe) (HF-synthesized)	Langmuir	25	115	Hasan et al. (2012)
	Surfactant-modified zeolite composite	Langmuir	25	16	Smiljanic et al. (2021)
	P-doped microporous carbon	Langmuir, Freundlich	32	21	Pap et al. (2021)
	Ag^0@reduced graphene oxide	Freundlich, Dubinin-Radushkevich	25	229	Mondal et al. (2020)
	Nano-Graphene oxide	Dubinin-Radushkevich	25	22	Ciğeroğlu et al. (2020)
	Polyamidoamine-grafted halloysite	Langmuir	25	8	Kurczewska et al. (2020)
	Magnetic quaternized dextrin ionomer	Freundlich	–	137	Shirkavand et al. (2019)
	γ-FeOOH	Langmuir	25	28	Li et al. (2018)
	Ionic liquid-impregnated sepabeads SP850	Freundlich	23	59	Wieszczycka et al. (2017)

the literature. Notably, MIL-100($FeSO_4$) registered a greater adsorptive potential as compared to the conventional MIL-100(Fe), which has been synthesized with the extremely hazardous hydrofluoric acid.

3.5. Kinetic modeling

The adsorption kinetics is concerned with the measured rate of adsorptive uptake by the solid adsorbent, as portrayed in Fig. 2. The accurate assessment of the best mathematical models, represented by the kinetic rate curves, is necessary as a crucial input to the adsorption simulation program code, needed for the process operation design. While the mechanistic models provide fundamental insight, empirical models are even more practical for the actual implementation purpose. In this sense, the kinetic data have been fitted to two lumped kinetic models, the pseudo-first order (PFO) and pseudo-second order (PSO) rate laws. Both PFO and PSO consider the surface binding as the rate-limiting step, that is usually the case when the interaction is chemical in nature. The derivations of these two pseudo-order models assume that: (1) The adsorbate binds to well-defined active sites of the adsorbent surface, with no lateral interaction between adsorbed species; (2) the profile of adsorption energy illustrates a homogeneous distribution; (3) the maximum adsorptive uptake is achieved when the adsorbent surface is saturated with a monolayer of adsorbate; (4) the concentration of the adsorbates in the adjoining aqueous plane surrounding the solid adsorbent remains constant; and (5) the adsorbate uptake is governed by n-th order rate equation, where $n = 1$ for PFO and $n = 2$ for PSO. The general equation can be expressed by:

$$\frac{dq_t}{dt} = k_n(q_e - q_t)^n \tag{7}$$

where q_t is the adsorptive uptake at time t (min); q_e is the equilibrium uptake (mg/g), and k_n is the pseudo n-th order rate constant. The PFO rate law is given by $n = 1$, while the PSO rate law results when $n = 2$. By integrating and rearranging Eq. (7), the PFO and PSO rate are presented as:

PFO: $$\ln(q_e - q_t) = \ln q_e - k_1 t \quad (7a)$$

PSO: $$\frac{t}{q_t} = \frac{1}{k_2 q_e^2} + \frac{t}{q_e} \quad (7b)$$

The plot of $\ln(q_e - q_t)$ vs k_1 and a plot of t/q_t vs t were constructed for the derivation of q_e, k_1, and k_2 from the slope and the y-intercept. The PSO linear plots have been given in Fig. 2 (c, d), and the kinetic parameters are summarized in Table 4. From the presented findings, the coefficients of determination of PSO fitting ($R^2 > 0.99$) were considerably higher than the PFO fitting, and the q_e values deduced from the PSO fitting were much closer to the experimental values, to verify the better fit to the PSO rate law. In other words, the adsorption process proceeded in such a way that the adsorptive uptake rate was proportional to the remaining available sites raised to the power of two. The compliance with the PSO kinetics agrees satisfactorily with the mainstream literature findings for the adsorption of MB and NPX.

3.6. Effect of ionic strength, water matrices, and simulated wastewater

The effects of ionic strength were examined to elucidate the adsorption mechanism, and verify the robustness of MIL-100($FeSO_4$) with the possible interference from the aqueous salinity. Identification of the effects of different saline species is vital to shed light on the adsorptive interaction, and the practical worth of the adsorbent for the treatment of different wastewaters. Six types of salts commonly present in the natural waterways were adopted for the evaluation of the adsorptive behavior under the interference of aqueous salinity. The exact degree of salinity impact differs from system to system, and relies on a host of intertwined factors, specifically the adsorbent, adsorbate, salt, and environmental settings. From Fig. 5(a, b), the adsorptive uptake of MB was found less vulnerable to salt disturbance than NPX. In the most detrimental salt species – Na_2CO_3 at 5 mM, the MB uptake could be sustained at 68% of the pristine capacity, while approximately 90% of reduction was found for the adsorptive uptake of NPX. The equilibrium uptake of MB took a boost of 20–40% in the presence of NaCl, $MgCl_2$, $NaNO_3$ or Na_2SO_4, while the adsorptive uptake of NPX remained almost unchanged only in the NaCl and $MgCl_2$ solutions. High electrolyte concentration is known to shield the electric double layer of the charged solid surface, and weaken the electrostatic attraction towards the opposite-charged organic adsorbates (Zhang et al., 2019). Meanwhile, the presence of these extremely soluble ionic electrolyte species may reduce the solubility of the organic adsorbates, but strengthen the hydrophobic interactions between the targeted adsorbates and adsorbent surface. Apparently, MB is more amenable to this effect, as its hydrophobic attraction towards MIL-100($FeSO_4$) could be amplified by the four tested salts. These findings indicate the presence of hydrophobic interactions, mainly in the form of $\pi - \pi$ electron donor–acceptor interaction between MB and MIL-100($FeSO_4$).

The MB uptake took a dip (~7–17%) in the NH_4Cl solutions, while the uptake of NPX was reduced by 13–17% at the 50 mM strength of $NaNO_3$, Na_2SO_4 and NH_4Cl. Na_2CO_3 (50 mM) was detrimental to both adsorbates, leaving only 38% of the pristine capacity for MB and 3% for NPX. Unlike the mono-atomic ions in the two-element salts, these O- and N-bearing polyatomic ions, with lone pairs of free electrons, could impose additional impact to the coordinatively unsaturated sites (CUS) of the adsorbent, such as the open Fe^{III} sites of the metal nodes of MIL-100($FeSO_4$). The uptake reduction in the saline solutions could be a sign of CUS coordination being a driving adsorption mechanism of the targeted adsorbates. The preferential coordination of these mobile polyatomic ionic ligands to the CUS of MIL-100($FeSO_4$) stripped the organic adsorbates from the binding sites. In a more complicated manner, the presence of concentrated Na_2CO_3 in the aqueous solution would enhance the solution alkalinity to a pH between 10 and 11. This alkalinization effect was seen to have jeopardized the adsorptive uptake of NPX drastically. Furthermore, the CO_3^{2-}, NO_3^- and SO_4^{2-} anions, by virtue of their structural resemblance to the CO_2^- in NPX, may bind competitively to MIL-100($FeSO_4$) by mimicking the adsorptive behavior of NPX.

The great performance for the laboratory findings under controlled conditions could not be necessarily translated into the similar behavior in the practical real settings. Therefore, the practical utility of MIL-100($FeSO_4$) was further examined using the real water samples. For this purpose, tap water and lakewater samples were spiked with the target adsorbates to be

Table 4 Kinetic parameters for the adsorptive uptakes of MB and NPX onto MIL-100($FeSO_4$) at 30 °C.

			Pseudo-first order			Pseudo-second order		
	C_o (mg/L)	Experimental uptake, q_{exp} (mg/g)	k_1(x10^2) (1/min)	q_e (mg/g)	R^2	k_2(x10^4) (g/mg·min)	q_e (mg/g)	R^2
MB	50	77.87	1.617	33.46	0.944	18.336	78.42	0.998
	100	132.27	1.736	58.03	0.902	10.207	133.66	0.998
	200	225.50	1.433	108.45	0.905	5.320	225.89	0.997
	300	279.45	1.650	121.31	0.965	5.210	282.74	0.998
	400	312.76	1.652	125.69	0.934	5.082	314.06	0.999
	500	341.79	1.595	137.15	0.890	5.060	341.74	0.998
NPX	10	19.43	0.997	6.929	0.879	85.176	19.77	0.999
	20	37.36	1.239	15.206	0.884	32.526	38.39	0.999
	40	71.34	1.300	51.109	0.990	7.160	74.45	0.996
	60	98.21	1.372	72.050	0.981	5.300	102.55	0.996
	80	119.54	1.526	95.035	0.987	4.352	125.71	0.997
	100	130.15	1.427	92.234	0.976	3.979	135.42	0.997

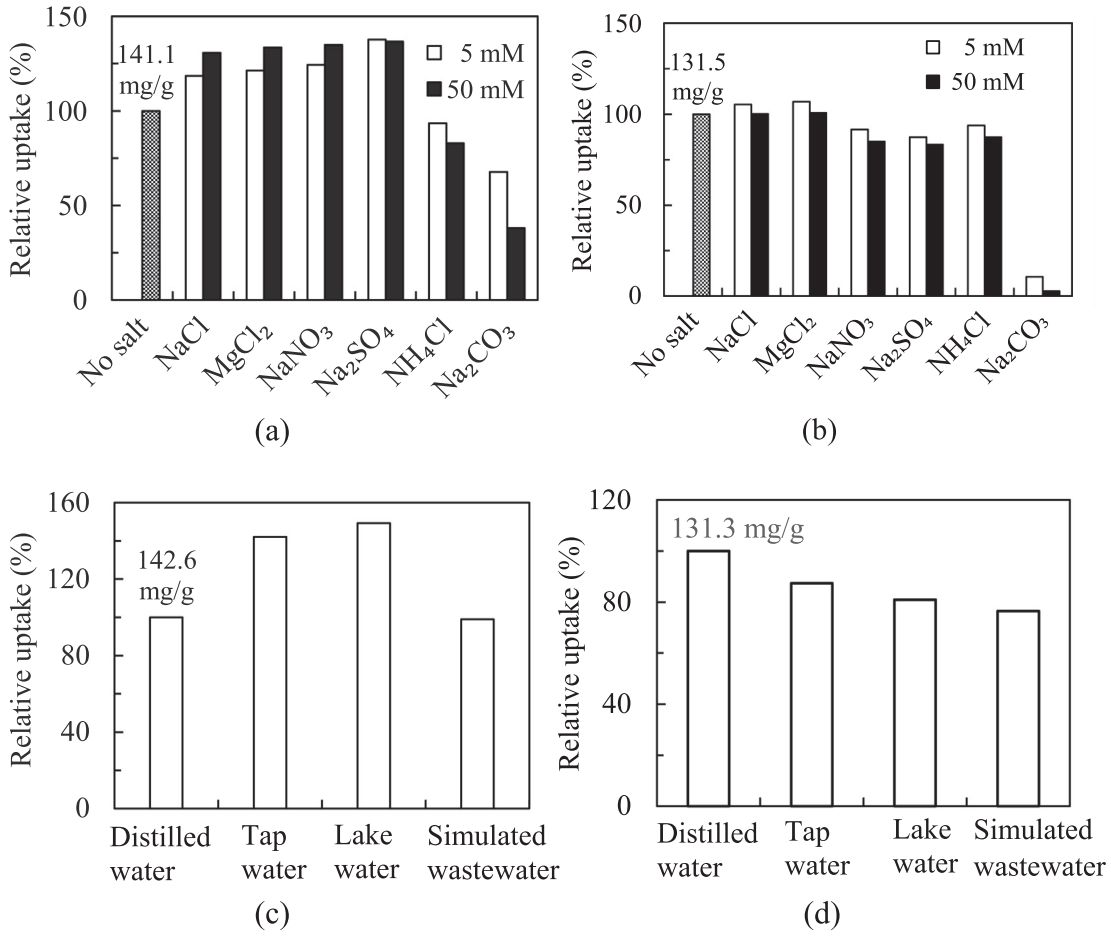

Fig. 5 (a, b) Effect of ionic strength for the adsorptive uptake of MB and NPX onto MIL-100($FeSO_4$), and (c, d) real waters and simulated wastewater studies (T = 30 °C, m/V = 0.5 g/L, C_o = 100 mg/L).

treated with MIL-100($FeSO_4$). The lakewater samples contain a diverse array of water matrix species, while tap water represents a treated freshwater, with trace amounts of residual disinfectants and disinfection by-products. These complex water matrices could impact the adsorptive uptake of the targeted adsorbates negatively. It was surprising from Fig. 5(c) and (d) that the adsorptive uptake of MB onto MIL-100($FeSO_4$) has increased over 40% in tap water and lakewater as compared to the ideal case of distilled water. This acquired finding ascertained the positive response of MB adsorption to the presence of different water matrix constituents, including Na^+, Cl^-, NO_3^-, and SO_4^{2-} electrolytes, in agreement with the earlier findings on ionic strength effect. Likewise, the adsorptive uptake of NPX has been verified to be more vulnerable to the salt deterioration implication in the real water samples. However, the variation of the adsorptive performance was not drastically affected, and the equilibrium uptake could still be sustained above 80% of the laboratory uptake in these real samples. This deterioration in these actual environment water samples could be driven by the competitive adsorptive interaction with different natural organic species, specifically the dissolved organic matters and humic substances, which took place and partially accounted for the performance drop.

The adsorptive behavior has been additionally tested using the simulated dye and pharmaceutical wastewaters. The synthetic MB wastewater composition (Table S3) was typical of a textile effluent (Parshetti et al., 2014), while the NPX wastewater (Table S4) was imitative of a pharmaceutical discharge (Wieszczycka et al., 2017). Similar with the commercial textile effluent, the MB-loaded wastewater contains huge loads of salts, surfactants, acids and bases needed during the dyeing process. The total ionic strength contributed by all the non-coloring ionic species was overwhelming, with a total concentration of 8500 mg/L against the MB strength of 100 mg/L. It was surprisingly delightful to indicate that the adsorptive uptake of MB could be maintained above 98% that it attained in the distilled water. Conversely, the uptake of NPX at 100 mg/L slumped to 76% of the laboratory uptake under the interference of 540 mg/L of the total ionic strength. Considering the strong interfering effects of multiple wastewater constituents, that are polyatomic O-containing with electrical charge, and coordinating lone pairs of electrons similar to the COO^- moiety in NPX, the adsorptive performance of MIL-100($FeSO_4$) was deemed robust and laudable. From the evaluation, it could be concluded that the adsorptive potential of MIL-100($FeSO_4$) was not significantly crippled by different aqueous matrices, ionic species and natural organic compounds, to signify it to be a promising candidate beyond the laboratory scale for water purification applications.

3.7. Regeneration analysis

Regeneration is a critical element in managing the adsorption process economics in terms of material costs for real industrial application. In the usual literature findings, the regeneration of MB- or NPX-saturated adsorbents has been attempted by means of chemical elution or thermal treatment, while the eluants that have been used for the chemical treatment are typically mineral acids, bases, salts, or organic solvents. In this work, the regeneration step for the exhausted MIL-100 ($FeSO_4$) was performed by adopting the "ultrasound-aided solvent stripping" strategy. This strategy is inspired by the facts that (i) polar organics dissolve well in polar organic solvents, and (ii) ultrasound aids in breaking molecular interactions and facilitates solutes dispersion. To preserve the "eco-friendliness" of the water-synthesized iron MOF, two most benign organic solvents, with different polarity: ethanol and acetone were adopted as the regenerants to desorb the immobilized adsorbates from the adsorbent surface. While both solvents were found good in terms of regeneration efficiency (Fig. 6), ethanol appeared to be a slightly better choice. MIL-100($FeSO_4$) could be reused for at least 5 times, with a preservation of over 95% of the pristine capacity for MB, and approximately 85% for NPX. Similar MB regeneration efficiency has been reported for up to 3 cycles by using ethanolic $HCl_{(aq)}$ elution (Luo et al., 2017), 5 cycles by acidified H_2O (Xiong et al., 2020), 2 cycles by 190 °C hydrothermal carbonization (Zhou et al., 2018), and recently, 6 cycles by 500 °C calcination (Sun et al., 2020). Comparatively, this work refrained from using mineral acids, bases, or excessive heating for the regeneration process, due to the corrosiveness or energy-intensiveness. Moreover, thermal regeneration is time-consuming (1–12 h), and it requires a continuous nitrogen gas flow during the application (Zhou et al., 2018; Hu et al., 2019; Zhou et al., 2019; Guo et al., 2020). In contrast, the desorption agents applied for the regeneration step, ethanol and acetone, may not only offer high regenerative potential, but are commonly available and cost effective. Post-adsorption XRD analysis showed that MIL-100($FeSO_4$) remained structurally stable after the ethanol regeneration (Fig. 1(b)). With the simple-swift regeneration procedure, MIL-100($FeSO_4$) promises sufficient capability, stability and durability for multicyclic purification of wastewater.

3.8. Thermodynamics analysis

The adsorption thermodynamics is concerned with the inherent energy changes during the adsorption interaction, and therefore represents a fundamental characterization of an adsorption system. By quantifying the macroscopic energy changes in terms of energy-related parameters, thermodynamic analysis outlines the adsorbent-adsorbate interactive mechanisms, and provides a better understanding on the adsorption behavior at the microscopic level. To examine the process energetics, thermodynamic analysis was conducted to quantify three important thermodynamic parameters: Gibbs free energy change (ΔG), enthalpy change (ΔH), and entropy change (ΔS) (Levine, 2009):

$$K_d = \frac{q_e m}{C_e V} = Q_0 K_L \frac{m}{V} \tag{8}$$

$$\Delta G = -RT \ln K_d \tag{9a}$$

$$\Delta G = \Delta H - T\Delta S \tag{9b}$$

where K_d is the distribution constant, T is the temperature (K) and R is the universal gas constant (8.314×10^{-3} kJ/mol·K). A plot of ΔG vs T yields the slope as $-\Delta S$ and the y-intercept as ΔH, as summarized in Table 5.

The negative values of ΔG suggested that the adsorption process took place spontaneously within the studied conditions range. The positive ΔH indicated that the adsorption was endothermic in nature, while the positive ΔS pointed to an entropy increase within the adsorption system. The phenomenon could be reasonably deduced from these thermodynamic parameters. As a requirement for the binding interaction in the aqueous medium, the MIL-100($FeSO_4$) surface and the adsorbate molecules need to be desolvated in the aqueous medium. The most obvious example is the displacement of water molecules coordinated to the unsaturated Fe^{III} sites of the inorganic building blocks of MIL-100($FeSO_4$) framework (Section 3.9). Higher temperature could facilitate this desolvation process, leading to a higher process spontaneity with a more negative ΔG. The solid–liquid interface of MOF-MB fixation showed a higher degree of disorderliness and randomness, as compared to the individually H_2O-solvated states of MIL-100($FeSO_4$) and MB. This is the driving

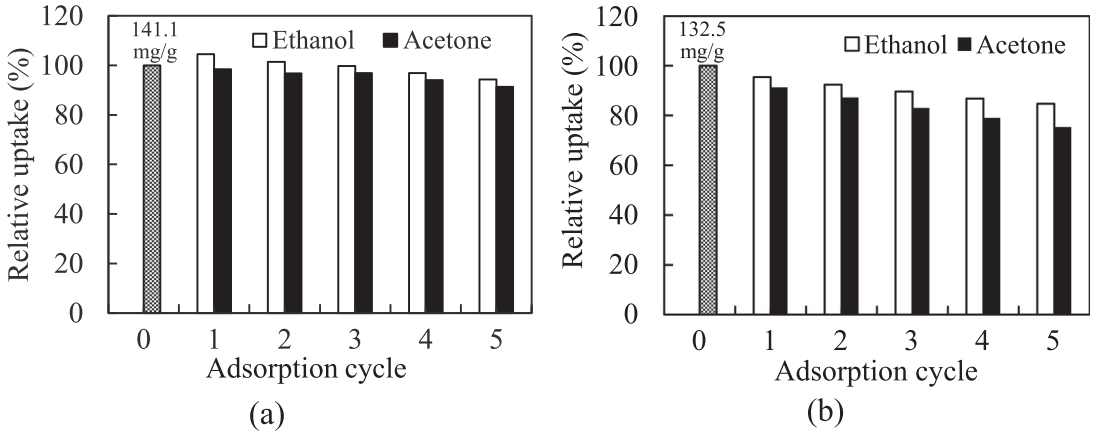

Fig. 6 The regenerative potential for the adsorption of (a) MB and (b) NPX onto MIL-100($FeSO_4$) via ultrasound-aided solvent stripping technique (T = 30 °C, m/V = 0.5 g/L, C_o = 100 mg/L).

Table 5 Thermodynamic parameters for the adsorptive uptakes of MB and NPX onto MIL-100($FeSO_4$).

	Temperature (K)	ΔG (kJ/mol)	ΔH (kJ/mol)	ΔS (J/mol·K)
MB	303	−3.13	21.81	82.31
	313	−3.94		
	323	−4.78		
NPX	303	−6.68	−5.42	3.77
	313	−6.60		
	323	−6.52		

force of the rising entropy ($\Delta S > 0$) during the binding of dye molecules to MOF. Considering the adverse effect of the positive ΔH on the process spontaneity, the entropy increase is the major thermodynamic driver for the adsorptive uptake of MB onto MIL-100($FeSO_4$).

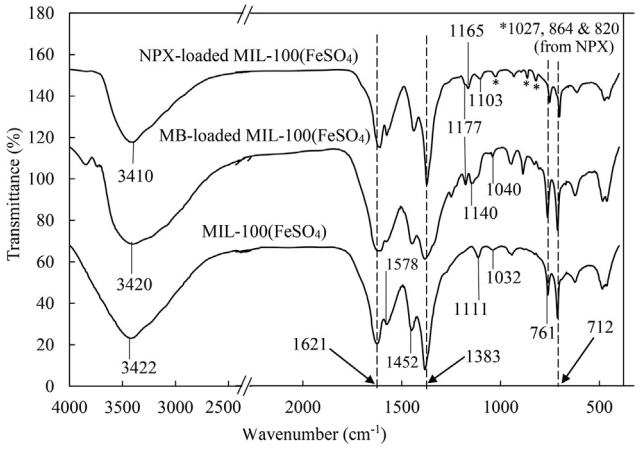

Fig. 7 FTIR spectra of MB-loaded MIL-100($FeSO_4$) and NPX-loaded MIL-100($FeSO_4$), in comparison to the fresh MIL-100 ($FeSO_4$).

With a larger $|\Delta G|$, the adsorptive uptake of NPX was more energetically favorable than the MIL-100($FeSO_4$)/MB system. Sparingly soluble in water, NPX is more hydrophobic than MB, and therefore the aromatic rings were greatly inclined to the interaction with the hydrophobic benzene rings of the MOF framework for higher thermodynamic stability. The negative ΔH indicated the exothermic nature of the NPX-MIL-100($FeSO_4$) interaction, due to the hydrophobic nature of the NPX molecules, which were mildly solvated in the aqueous medium, and the energy required for the desolvation was outweighed by the heat release during the surface binding, resulting in a net heat release. The thermodynamic driving force for the NPX-MIL-100($FeSO_4$) adsorption is primarily driven by the enthalpy, and secondarily, the entropy.

3.9. Adsorption mechanism

The multiple interactions between the adsorbent-adsorbate system are according to the unique features, or types of the surrounding aqueous conditions. These interactions, susceptible to the changing process conditions could be proven experimentally. From the solution pH and salinity studies, electrostatic attraction could be confidently proposed to be the most prevalent mechanism governing the adsorption of MB onto MIL-100($FeSO_4$). In the presence of salting out effect, the $\pi - \pi$ interactions between the benzene rings of TMA within the MOF framework, and the guest MB molecules could be identified to be the major dye-MOF binding interaction. The $\pi - \pi$ interactions could also be deduced for the adsorption of NPX, judging from its much lower solubility but a higher $|\Delta G|$. This proposition was reinforced by the post-adsorption FTIR analysis. From Fig. 7, the peaks of the aromatic C═C and C─C bond deformations at 1032 cm^{-1}, and the signal at 1111 cm^{-1} of MIL-100($FeSO_4$) have shifted to higher wavenumbers after the adsorption process. For the MB-loaded sample, these deformation peaks for the MB-loaded sample have shifted to 1040 and 1140 cm^{-1} respectively, while the corresponding peak positions for the NPX loaded sample are 1103 cm^{-1} and 1165 cm^{-1}. A new shoulder

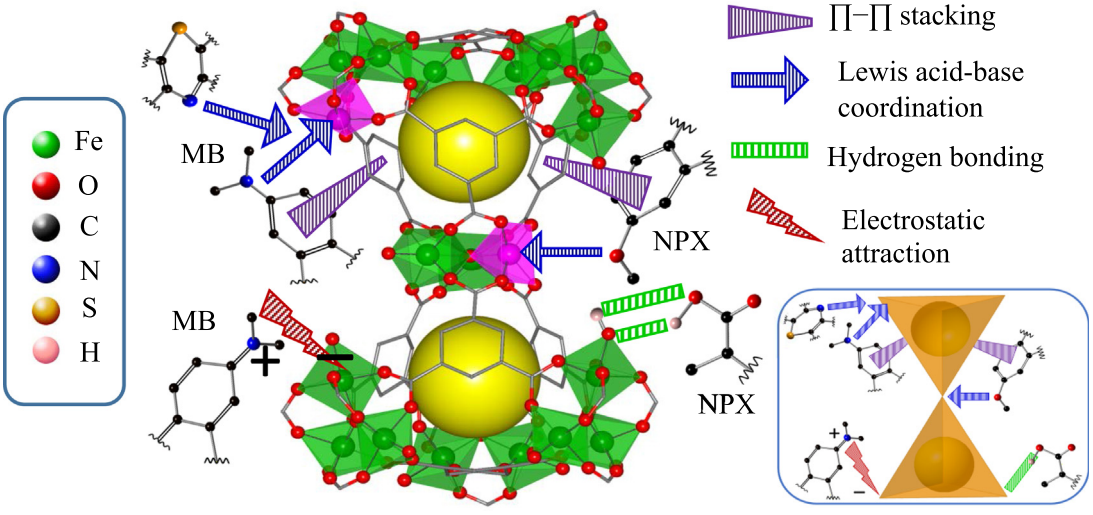

Scheme 2 Proposed mechanism for the adsorption of MB and NPX onto MIL-100($FeSO_4$). Bottom-right inset depicts an overall simplified view of the two corner-shared supertetrahedrons interacting with the adsorbate pollutants.

peak was found at 1177 cm^{-1} after the adsorption of both MB and NPX, indicating a change in the in-plane C—H bending of the benzene rings after the adsorptive interaction. Similarly, the shoulder peaks at 1578 cm^{-1} and 1452 cm^{-1}, belonging to the MOF's aromatic C=C stretching, have either turned less intense [relative to v_{as}(O=C—O^-) and v_s(O=C—O^-) bands of the MOF] or undergone a shift of wavenumber. The changing FTIR pattern could strongly suggest the host–guest aromatic $\pi - \pi$ interaction between the benzene rings of MIL-100($FeSO_4$) and the targeted adsorbate molecules. The OH band at 3422 cm^{-1} has shifted to 3410 cm^{-1} after the adsorption of NPX molecules, signifying the hydrogen bonding interaction, most probably between the terminal —OH of the iron(III) clusters, and the —O/—OH groups of NPX. This finding was well corroborated with the previous literature findings that H-bonding remains a preferred mode for the adsorptive uptake of O- or OH-rich pharmaceutical compounds in the aqueous medium (Song et al., 2017; Song and Jhung, 2017).

Another possible mechanism was the Lewis acid – Lewis base coordination between the (—$N(CH_3)_2$) groups of MB, or the (C—O—C) groups of NPX, with the coordinatively unsaturated iron sites. The lone pair electron-rich N and O are coordinating moieties that could bind efficiently to the electron-deficient sites, like the open metal sites of MOFs. Although the Lewis acidic open metal sites were occupied by water molecules in the aqueous media, the possibility of the stronger Lewis base (—$N(CH_3)_2$) and (C—O—C) in substituting the coordinated water molecules could not be excluded (Huo and Yan, 2012). The Lewis acid-Lewis base coordination mechanism postulated herein was well correlated with the ionic strength study, in which the polyatomic O- and N-bearing electrolytes may have significantly interfered with the MB/NPX-MIL-100($FeSO_4$) coordination, leading to a competitive adsorption effect (Section 3.6). For a better visualization, the plausible mechanisms for the adsorption of MB and NPX onto MIL-100($FeSO_4$) have been graphically proposed in Scheme 2.

4. Conclusion

The preparation of an eco-friendly iron-based MOF, MIL-100($FeSO_4$), via a heatless, green and hassle-free technique has been successfully accomplished. The MOF demonstrated excellent adsorptive performance for both cationic (methylene blue, MB) and anionic (naproxen, NPX) adsorbates. The monolayer adsorption capacity ranged from 568.1 to 1099.4 mg/g for MB, and from 123.3 to 148.8 mg/g for NPX. The adsorption data were best-fitted to the Langmuir-Freundlich isotherm model and pseudo-second order kinetic equation. The adsorption was endothermic for MB, but exothermic for NPX. The adsorption mechanism was driven by aromatic $\pi - \pi$ stacking, Lewis acid-base interaction, and further enhanced by electrostatic attraction for MB, and by hydrogen bonding for NPX. The adsorptive performance was minimally affected by the solution ionic strength, aqueous matrices, high-strength simulated wastewater and contaminated environmental water samples. MIL-100($FeSO_4$) showed high reusability potential via simple ethanol washing. Conclusively, the sustainably synthesized MIL-100($FeSO_4$) could prevail to be the next-generation green adsorbent for effective water purification.

Declaration of Competing Interest

The authors declare that they have no known competing financial interests or personal relationships that could have appeared to influence the work reported in this paper.

Acknowledgement

The authors acknowledge the financial support provided by Universiti Sains Malaysia under the Research University Individual (RUI) Grant (Project No. 1001/PREDAC/8011139) entitled "Facile Synthesis of Cellulose Nanocrystals Integrated Magnetic-Metal Organic Framework (MOF) Composites for Wastewater Remediation".

Appendix A. Supplementary material

Supplementary data to this article can be found online at https://doi.org/10.1016/j.arabjc.2021.103359.

References

Aguiar, L.W., Otto, G.P., Kupfer, V.L., Fávaro, S.L., Silva, C.T.P., Moisés, M.P., et al, 2020. Simple, fast, and low-cost synthesis of MIL-100 and MIL-88B in a modified domestic microwave oven. Mater. Lett. 276, 128127.

Alomar, T.S., AlMasoud, N., Sharma, G., Alothman, Z.A., Naushad, M., 2021. Incorporation of trimetallic nanoparticles to the SiO_2 matrix for the removal of methylene blue dye from aqueous medium. J. Mol. Liq. 336, 116274.

Bayazit, Ş.S., Şahin, S., 2020. Acid-modulated zirconium based metal organic frameworks for removal of organic micropollutants. J. Environ. Chem. Eng. 8, 103901.

Cai, J., Wang, X., Zhou, Y., Jiang, L., Wang, C., 2016. Selective adsorption of arsenate and the reversible structure transformation of the mesoporous metal-organic framework MIL-100(Fe). Phys. Chem. Chem. Phys. 18, 10864–10867.

Cheng, Y., Xu, L., Jiang, Z., Liu, C., Zhang, Q., Zou, Y., et al, 2021. Feasible low-cost conversion of red mud into magnetically separated and recycled hybrid $SrFe_{12}O_{19}$@NaP1 zeolite as a novel wastewater adsorbent. Chem. Eng. J. 417, 128090.

Ciğeroğlu, Z., Özdemir, O.K., Şahin, S., Haşimoğlu, A., 2020. Naproxen adsorption onto graphene oxide nanopowders: Equilibrium, kinetic, and thermodynamic studies. Water, Air, Soil Pollut. 231, 101.

Freundlich, H.M., 1906. Over the adsorption in solution. J. Phys. Chem. A 57, 385–470.

Guesh, K., Caiuby, C.A.D., Mayoral, Á., Díaz-García, M., Díaz, I., Sanchez-Sanchez, M., 2017. Sustainable preparation of MIL-100 (Fe) and its photocatalytic behavior in the degradation of methyl orange in water. Cryst. Growth Des. 17, 1806–1813.

Guo, F., Jiang, X., Li, X., Jia, X., Liang, S., Qian, L., 2020. Synthesis of MgO/Fe_3O_4 nanoparticles embedded activated carbon from biomass for high-efficient adsorption of malachite green. Mater. Chem. Phys. 240, 122240.

Han, L., Qi, H., Zhang, D., Ye, G., Zhou, W., Hou, C., et al, 2017. A facile and green synthesis of MIL-100(Fe) with high-yield and its catalytic performance. New J. Chem. 41, 13504–13509.

Hasan, Z., Jeon, J., Jhung, S.H., 2012. Adsorptive removal of naproxen and clofibric acid from water using metal-organic frameworks. J. Hazard. Mater. 209–210, 151–157.

He, B.S., Wang, J., Liu, J., Hu, X.M., 2017. Eco-pharmacovigilance of non-steroidal anti-inflammatory drugs: Necessity and opportunities. Chemosphere 181, 178–189.

Horcajada, P., Surble, S., Serre, C., Hong, D.Y., Seo, Y.K., Chang, J. S., et al, 2007. Synthesis and catalytic properties of MIL-100(Fe), an iron(III) carboxylate with large pores. Chem. Commun., 2820–2822

Hu, W., Xie, Y., Lu, S., Li, P., Xie, T., Zhang, Y., et al, 2019. One-step synthesis of nitrogen-doped sludge carbon as a bifunctional material for the adsorption and catalytic oxidation of organic pollutants. Sci. Total Environ. 680, 51–60.

Huo, S.H., Yan, X.P., 2012. Metal–organic framework MIL-100(Fe) for the adsorption of malachite green from aqueous solution. J. Mater. Chem. 22, 7449–7455.

Juan-Alcañiz, J., Gielisse, R., Lago, A.B., Ramos-Fernandez, E.V., Serra-Crespo, P., Devic, T., et al, 2013. Towards acid MOFs – catalytic performance of sulfonic acid functionalized architectures. Catal. Sci. Technol. 3, 2311.

Julien, P.A., Mottillo, C., Friščić, T., 2017. Metal–organic frameworks meet scalable and sustainable synthesis. Green Chem. 19, 2729–2747.

Kurczewska, J., Cegłowski, M., Schroeder, G., 2020. PAMAM-halloysite Dunino hybrid as an effective adsorbent of ibuprofen and naproxen from aqueous solutions. Appl. Clay Sci. 190, 105603.

Langmuir, I., 1916. The constitution and fundamental properties of solids and liquids. Part i. Solids. J. Am. Chem. Soc. 38, 2221–2295.

Levine, I.N., 2009. Physical Chemistry. McGraw-Hill, New York.

Li, Z., Liu, G., Su, Q., Jin, X., Wen, X., Zhang, G., et al, 2018. Kinetics and thermodynamics of NPX adsorption by γ-FeOOH in aqueous media. Arab. J. Chem. 11, 910–917.

Luo, X.P., Fu, S.Y., Du, Y.M., Guo, J.Z., Li, B., 2017. Adsorption of methylene blue and malachite green from aqueous solution by sulfonic acid group modified MIL-101. Microporous Mesoporous Mater. 237, 268–274.

Luo, Y., Tan, B., Liang, X., Wang, S., Gao, X., Zhang, Z., et al, 2019. Dry gel conversion synthesis of hierarchical porous MIL-100(Fe) and its water vapor adsorption/desorption performance. Ind. Eng. Chem. Res. 58, 7801–7807.

Minisy, I.M., Salahuddin, N.A., Ayad, M.M., 2021. Adsorption of methylene blue onto chitosan–montmorillonite/polyaniline nanocomposite. Appl. Clay Sci. 203, 105993.

Mondal, S., Patel, S., Majumder, S.K., 2020. Bio-extract assisted in-situ green synthesis of Ag-RGO nanocomposite film for enhanced naproxen removal. Korean J. Chem. Eng. 37, 274–289.

Nie, Z.J., Guo, Q.F., Xia, H., Song, M.M., Qiu, Z.J., Fan, S.T., et al, 2021. Cyclodextrin self-assembled graphene oxide aerogel microspheres as broad-spectrum adsorbent for removing dyes and organic micropollutants from water. J. Environ. Chem. Eng. 9, 104749.

Oun, A.A., Kamal, K.H., Farroh, K., Ali, E.F., Hassan, M.A., 2021. Development of fast and high-efficiency sponge-gourd fibers (*Luffa cylindrica*)/hydroxyapatite composites for removal of lead and methylene blue. Arab. J. Chem. 14, 103281.

Ozer, D., Icten, O., Altuntas-Oztas, N., Zumreoglu-Karan, B., 2020. MIL-100(Fe) metal–organic framework catalyzed oxidation of phenol revisited: dark-Fenton activity of the catalyst. Res. Chem. Intermed. 46, 909–922.

Pap, S., Taggart, M.A., Shearer, L., Li, Y., Radovic, S., Turk Sekulic, M., 2021. Removal behaviour of NSAIDs from wastewater using a P-functionalised microporous carbon. Chemosphere 264, 128439.

Parshetti, G.K., Chowdhury, S., Balasubramanian, R., 2014. Hydrothermal conversion of urban food waste to chars for removal of textile dyes from contaminated waters. Bioresour. Technol. 161, 310–319.

Pathania, D., Sharma, S., Singh, P., 2017. Removal of methylene blue by adsorption onto activated carbon developed from *Ficus carica* bast. Arab. J. Chem. 10, S1445–S1451.

Peng, Y., Zhang, Y., Huang, H., Zhong, C., 2018. Flexibility induced high-performance MOF-based adsorbent for nitroimidazole antibiotics capture. Chem. Eng. J. 333, 678–685.

Ryu, U., Jee, S., Rao, P.C., Shin, J., Ko, C., Yoon, M., et al, 2021. Recent advances in process engineering and upcoming applications of metal-organic frameworks. Coord. Chem. Rev. 426, 213544.

Saxena, M., Lochab, A., Saxena, R., 2021. Asparagine functionalized MWCNTs for adsorptive removal of hazardous cationic dyes: Exploring kinetics, isotherm and mechanism. Surf. Interfaces 25, 101187.

Seetharaj, R., Vandana, P.V., Arya, P., Mathew, S., 2019. Dependence of solvents, pH, molar ratio and temperature in tuning metal organic framework architecture. Arab. J. Chem. 12, 295–315.

Shirkavand, F., Beyki, M.H., Shemirani, F., 2019. Enhanced naproxen removal over magnetic quaternized dextrin ionomer: response surface optimization, kinetics, isotherm and comparing study. Desalin. Water Treat. 143, 333–351.

Sips, R., 1948. On the structure of a catalyst surface. J. Chem. Phys. 16, 490–495.

Smiljanic, D., de Gennaro, B., Dakovic, A., Galzerano, B., Germinario, C., Izzo, F., et al, 2021. Removal of non-steroidal anti-inflammatory drugs from water by zeolite-rich composites: The interference of inorganic anions on the ibuprofen and naproxen adsorption. J. Environ. Manage. 286, 112168.

So, P.B., Chen, H.T., Lin, C.H., 2020. *De novo* synthesis and particle size control of iron metal organic framework for diclofenac drug delivery. Microporous Mesoporous Mater. 309, 110495.

Song, J.Y., Bhadra, B.N., Jhung, S.H., 2017. Contribution of H-bond in adsorptive removal of pharmaceutical and personal care products from water using oxidized activated carbon. Microporous Mesoporous Mater. 243, 221–228.

Song, J.Y., Jhung, S.H., 2017. Adsorption of pharmaceuticals and personal care products over metal-organic frameworks functionalized with hydroxyl groups: Quantitative analyses of H-bonding in adsorption. Chem. Eng. J. 322, 366–374.

Sultan, M., Mansor, E.S., Nagieb, Z.A., Elsayed, H., 2021. Fabrication of highly efficient nano-composite films based on ZnO-g-C_3N_4@ PAA-g-(HEC/PVA)-Fe^{3+} for removal of methylene blue dye from water. J. Water Process Eng. 42, 102184.

Sun, Z., Yang, J., Qi, Y., Wang, F., Hong, W., Li, H., et al, 2020. Facile preparation of hydroxyl-rich mesoporous magnesium silicate with excellent adsorption performance. Surf. Interfaces 20, 100519.

Tang, Y., Huang, H., Xue, W., Chang, Y., Li, Y., Guo, X., et al, 2020. Rigidifying induced fluorescence enhancement in 2D porous covalent triazine framework nanosheets for the simultaneously luminous detection and adsorption removal of antibiotics. Chem. Eng. J. 384, 123382.

Thommes, M., Kaneko, K., Neimark, A.V., Olivier, J.P., Rodriguez-Reinoso, F., Rouquerol, J., et al, 2015. Physisorption of gases, with special reference to the evaluation of surface area and pore size distribution (IUPAC Technical Report). Pure Appl. Chem. 87, 1051–1069.

Udayakumar, M., El Mrabate, B., Koós, T., Szemmelveisz, K., Kristály, F., Leskó, M., et al, 2021. Synthesis of activated carbon foams with high specific surface area using polyurethane elastomer templates for effective removal of methylene blue. Arab. J. Chem. 14, 103214.

Wieszczycka, K., Zembrzuska, J., Bornikowska, J., Wojciechowska, A., Wojciechowska, I., 2017. Removal of naproxen from water by ionic liquid-modified polymer sorbents. Chem. Eng. Res. Des. 117, 698–705.

Wu, X., Xiong, J., Liu, S., Cheng, J.H., Zong, M.H., Lou, W.Y., 2021. Investigation of hierarchically porous zeolitic imidazolate frameworks for highly efficient dye removal. J. Hazard. Mater. 417, 126011.

Xia, Y., Yao, Q., Zhang, W., Zhang, Y., Zhao, M., 2019. Comparative adsorption of methylene blue by magnetic baker's yeast and EDTAD-modified magnetic baker's yeast: Equilibrium and kinetic study. Arab. J. Chem. 12, 2448–2456.

Xiong, J., Zhang, D., Lin, H., Chen, Y., 2020. Amphiprotic cellulose mediated graphene oxide magnetic aerogels for water remediation. Chem. Eng. J. 400, 125890.

Yao, G., Liu, X., Zhang, G., Han, Z., Liu, H., 2021. Green synthesis of tannic acid functionalized graphene hydrogel to efficiently adsorb methylene blue. Colloids Surf. A: Physicochem. Eng. Asp. 625, 126972.

Zhang, Y., Zhu, C., Liu, F., Yuan, Y., Wu, H., Li, A., 2019. Effects of ionic strength on removal of toxic pollutants from aqueous media with multifarious adsorbents: A review. Sci. Total Environ. 646, 265–279.

Zhao, L., Tang, P., Sun, Q., Zhang, S., Suo, Z., Yang, H., et al, 2020. Fabrication of carboxymethyl functionalized β-cyclodextrin-modified graphene oxide for efficient removal of methylene blue. Arab. J. Chem. 13, 7020–7031.

Zhou, H., Yan, B., Lai, J., Liu, H., Ma, A., Chen, W., et al, 2018. Renewable biomass derived hierarchically porous carbonaceous sponges and their magnetic nanocomposites for removal of organic molecules from water. J. Ind. Eng. Chem. 58, 334–342.

Zhou, J., Zhang, C., Niu, T., Huang, R., Li, S., Sun, J., et al, 2019. Facile synthesis of reusable magnetic Fe/Fe_3C/C composites from renewable resources for super-fast removal of organic dyes: Characterization, mechanism and kinetics. Powder Technol. 351, 314–324.